

Laser Pulse Induced Second- and Third-Harmonic Generation of Gold Nanorods with Real-Time Time-Dependent Density Functional Tight Binding (RT-TDDFTB) Method

Sajal Kumar Giri¹ and George C. Schatz^{1, a)}

Department of Chemistry, Northwestern University, 2145 Sheridan Road, Evanston, Illinois 60208, United States

In this study, we investigate second- and third-harmonic generation processes in Au nanorod systems using the real-time time-dependent density functional tight binding (RT-TDDFTB) method. Our study focuses on computation of nonlinear signals based on the time dependent dipole response induced by linearly polarized laser pulses interacting with nanoparticles. We systematically explore the influence of various laser parameters, including pump intensity, duration, frequency, and polarization directions, on the harmonic generation. We demonstrate all the results using Au nanorod dimer systems arranged in end-to-end configurations, and disrupting the spatial symmetry of regular single nanorod systems crucial for second harmonic generation processes. Furthermore, we study the impact of nanorod lengths, which lead to variable plasmon energies, on the harmonic generation, and estimates of polarizabilities and hyper-polarizabilities are provided.

I. INTRODUCTION

The study of nonlinear optical processes at the nanoscale has gained substantial interest in recent years due to its importance in various fields, including microscopy,¹⁻³ optoelectronics,^{4,5} and biomedical applications.⁶⁻⁸ Among these phenomena, harmonic generation (HG) has emerged as an important process for manipulating light at the nanoscale.⁹⁻¹⁴ This process involves the nonlinear interaction between intense laser fields and matter, where the induced polarization scales nonlinearly with the interacting field amplitude, resulting in the emission of harmonics at integer multiples of the incident laser frequency.^{15,16}

Most of the past studies on HG have involved atomic¹⁷⁻¹⁹ or molecular^{20,21} systems. However, the generated signals are usually extremely weak, requiring very intense incident pulses. This is because the HG process involves multiple photons, and there is a low conversion efficiency associated with the weak light-matter coupling and a low density of states of the medium. There is an ongoing effort to identify ideal target systems for efficient HG processes. Recent experimental successes in HG on liquids,²² solids,²³ and nanostructures²⁴ have significantly enhanced the conversion efficiency beyond the limits of gas target systems.

Second and third harmonic generation processes are of particular interest due to their emerging potential applications that cannot be achieved using conventional linear absorption.^{25,26} Second harmonic generation (SHG) is a nonlinear optical process that involves the conversion of the fundamental frequency into second harmonics at doubled the frequency. SHG involving nanoparticles in solution involves the coherent excitation

of each particle. However, the contributions from the ensemble of particles that are irradiated involve an incoherent sum, leading to a process that is sometimes referred to as Hyper-Rayleigh scattering, but we will use the term SHG throughout this paper. Under the dipole approximation, which applies when the dimension of a particle is much smaller than the wavelength of the incident radiation, centrosymmetric particles are inactive in SHG experiments,^{15,16} as long as the particles remain much smaller than the wavelength of light. SHG emission from small nanoparticles is, therefore, available only for structures with asymmetric geometries, for example, a small metallic particle with the shape deviating from a perfect sphere.²⁷ Similarly, third harmonic generation (THG) involves the tripling of the incident frequency, and is allowed for spherical particles.^{15,16}

Noble metal nanoparticles, in particular, exhibit enhanced optical absorption due to collective excitation of conduction electrons when excited with a characteristic frequency of the particles, a phenomenon known as localized surface plasmon resonance (LSPR).^{28,29} These plasmonic resonances can significantly enhance the local electromagnetic field, thereby intensifying the nonlinear optical processes involved in HG. SHG³⁰⁻³⁶ and THG^{31,37-39} can be enhanced by several orders of magnitude due to the surface plasmon effects. Here, plasmonic excitation provides both stronger coupling and high state densities for the conversion of the incident photons into higher-energy harmonics. The unique tunability of nanoparticle plasmons allows for precise control over the harmonic generation process, offering opportunities for tailoring the spectral and spatial properties of generated harmonics. Moreover, plasmonic nanoparticles provide a significant advantage compared to harmonic generation from bulk solids in achieving phase matching conditions between the incident and generated harmonics, which is essential for an efficient harmonic emission.

^{a)}Electronic mail: g-schatz@northwestern.edu

Previous theoretical treatments of the optical properties of nanoparticles have employed several methods, including simulations based on Maxwell's equations,⁴⁰ mixed quantum-classical treatments,^{41–43} time-dependent density functional theory (TD-DFT)^{44–48} and semi-empirical methods^{49,50}. However, only a few of these methods have been used to determine HG properties for metallic nanoparticles. Finite-difference time-domain (FDTD) simulations offer a powerful tool for modeling the interaction of intense laser fields with nanoparticles, providing insights into the spatiotemporal evolution of electromagnetic fields and the resulting harmonic generation.^{51–56} As an alternative to electrodynamics, TD-DFT calculations provide a more rigorous picture of the electronic excitation and transitions in nanoparticles, elucidating the role of electronic structure in HG processes. However, computational efficiency is a major concern while using TD-DFT for nanoparticles. Alternatively, semi-empirical methods such as INDO/S provide computationally efficient approaches for investigating nonlinear optical processes in complex nanoparticle systems, however, computational constraints have still limited the exploration of large-scale applications.

Density functional tight binding (DFTB) method is a semi-empirical approach that shares similarities with the earlier INDO-based methods but is formulated within the framework of density functional theory (DFT), providing improved accuracy. Indeed, this method often generates results comparable to DFT but with significantly reduced computational costs, enabling efficient simulation of ground and excited state properties for larger complexes. Recent papers provide comprehensive details of the DFTB method.^{57,58} Previous studies have discussed the success of the DFTB method for the structures and thermodynamic properties of many systems, including bio-molecules,⁵⁹ metals,^{60–64} semiconductors,⁶⁵, etc. Furthermore, this method has now been extended to time-dependent versions that are especially efficient for describing the dynamics of nanoparticles that is induced by external laser fields. The accuracy of predictions using this method relies on the quality of parameters representing the Hamiltonian (H) and overlap (S) matrices, however, a number of successful applications to linear optical properties of noble metals have been presented using readily available parameters

In this work, we explore SHG and THG processes in end-to-end Au nanorod dimer systems induced by linearly polarized laser pulses using the real-time TD-DFTB method through the computation of time-dependent induced dipoles. This paper includes two major objectives: (a) to determine the feasibility of studying nonlinear optical processes for plasmonic nanoparticles by simulating real-time dynamics at the

atomistic level and (b) to assess the influence of laser pulse parameters on these processes. We present a comprehensive analysis of the effect of various laser parameters, including pump intensity, frequency, duration, and laser polarization direction, on the nonlinear optical phenomena. We also consider the influence of plasmon dephasing and damping on the results. Additionally, we investigate the impact of nanoparticle size, determining how the length of the nanorods affects the HG efficiency, and we report the polarizabilities and first and second hyper-polarizabilities for dimer systems calculated from the induced dipoles, including comparisons with the experiment. The results demonstrate that the real-time TD-DFTB provides a powerful tool for determining HG properties in plasmonic nanoparticles.

Throughout this paper, atomic units are utilized unless otherwise specified.

II. THEORY AND COMPUTATION

All computations in this study have been conducted using the DFTB+ code that works based on the DFTB method. We use auorg/auorg-1-1 Slater-Koster parameters for Au systems downloaded from the dftb.org site. This method provides a balance between accuracy and computational cost, making it particularly suitable for large-scale simulations. The accuracy of the DFTB calculations is typically comparable to that of the more rigorous DFT method while offering substantially reduced computational costs. However, it is important to note that the accuracy of these calculations can be influenced by various factors, including the empirical parameters used to describe the electronic structure. In addition to investigating ground state properties, we used this method to study excited state properties that is an extension of the method to the time domain. Furthermore, this method allows us to incorporate external electromagnetic fields explicitly to drive the dynamics through the field-matter interactions.

In real-time dynamics simulations within the DFTB framework, the evolution of the single particle electronic density matrix is governed by the Liouville von-Neumann equation.⁵⁸ The density matrix is propagated in time using

$$\dot{\rho} = -iS^{-1}[H, \rho]S^{-1}, \quad (1)$$

starting from an initial state defined by Hamiltonian (H_0), overlap (S_0), and density (ρ_0) matrices. Here S^{-1} represents the inverse of S . The above equation describes the propagation of the electronic density matrix over time where the interaction with an external field initiates transitions between electronic states. The Hamiltonian includes a field-matter coupling term through the dipole approximation $V_A(t) = -\boldsymbol{\mu} \cdot \mathbf{E}(t)$, where $\mathbf{E}(t)$ is the external field and $\boldsymbol{\mu} = \sum_A \Delta q_A \mathbf{R}_A(t)$ is the dipole moment

associated with atomic coordinate \mathbf{R}_A and charge Δq_A for atom A at time t . The external field takes the following form:

$$E_a(t) = \hat{e}_a E_p \exp(-(t - t_c)^2 / T_p^2) \sin(\omega_p t), \quad (2)$$

with peak amplitude E_p , center of the pulse t_c , pulse duration T_p , frequency ω_p , and polarization direction \hat{e}_a . By solving Eq.1 numerically, it becomes possible to track the dynamic behavior of the system as it evolves in real time. Although the light-matter interaction may trigger nuclear dynamics, our focus lies on the electronic dynamics for HG processes, hence we constrain nuclear motion in our simulation. This is a legitimate approximation as nuclei initially exhibit slow movement, and we only need to simulate dynamics up to 200 fs for the properties we are calculating.^{58,66,67} Nuclear dynamics becomes more relevant for materials over longer timescales.

To elucidate the process of HG in nanoparticles, we excite them with an intense laser pulse of the form given in Eq.2. The induced dipole $\mu_a(t) = \text{Tr}[(\hat{e}_a \cdot \boldsymbol{\mu})\rho(t)]$ oscillates in time coherently for an infinitely long time in the absence of dissipation, including all frequency modes that are activated through the interactions, including both fundamental and generated harmonics. The induced dipole can be expressed as⁶⁸

$$\begin{aligned} \mu_a(t) = & \mu_a^0 + \sum_b \int_{-\infty}^{\infty} dt_1 \alpha_{ab}(t - t_1) E_b(t_1) \\ & + \frac{1}{2!} \sum_{bc} \int \int_{-\infty}^{\infty} dt_1 dt_2 \beta_{abc}(t - t_1, t - t_2) E_b(t_1) E_c(t_2) \\ & + \frac{1}{3!} \sum_{bcd} \int \int \int_{-\infty}^{\infty} dt_1 dt_2 dt_3 \gamma_{abcd}(t - t_1, t - t_2, t - t_3) \\ & \times E_b(t_1) E_c(t_2) E_d(t_3) + \dots, \end{aligned} \quad (3)$$

where a, b, c and d denote Cartesian coordinates. α, β and γ are hyper-polarizability tensors representing the first, second, and third order responses, as determined by the polarizability and the first and second hyper-polarizabilities, respectively. In the above equation, μ_a^0 is the permanent dipole moment.

To provide a realistic description of the excited state dynamics that includes dephasing and relaxation due to electron-electron and electron-nuclear interactions, we introduce empirical damping to the dipole amplitude, effectively limiting the oscillation to a finite time.^{66,69} This damping function is chosen to be an exponential function of the form given in Eq.5, where τ controls the dephasing/damping rate. Throughout the paper we use $\tau = 20$ fs. This value is related to the Drude width and often this is considered to be ~ 0.1 eV corresponding to $\tau = 10$ fs.⁷⁰ This has been used in the past in electro-dynamics calculations to predict extinction spectra for spherical gold nanoparticles for wavelengths close to 520

nm, where the measured width of the plasmon is around 0.2 eV (where deviations between the two widths are due to effects not contained in the Drude model as well as uncertainties in determining values of the widths from the measured lineshape due to a nonresonant background). For rod-shaped particles where the plasmon is shifted to a longer wavelength (in the NIR), the Drude width based on fitting measured dielectric functions is usually given a smaller value, such as 0.02 eV.⁷¹ However, for rods that are large (10s of nm in diameter), the plasmon width based on electro-dynamics calculations is found to slowly decrease from 0.2 to 0.1 eV in going from 520 nm to over 1000 nm. This arises because radiative damping contributions broaden the plasmon beyond what it would be due to intrinsic damping, and there are also important frequency dispersion effects that control the linewidth.^{72,73} In the present application we are interested in using our electronic structure calculations for small rods to describe properties that can be connected to the behavior of large rods, so we use $\tau = 20$ fs as a value that is more realistic for the plasmon resonances we consider, but without putting in an explicit dependence of τ on plasmon wavelength. The influence of other values of τ will be presented later when we consider polarizability results.

The dipole oscillations are primarily dominated by the fundamental frequency of the laser excitation. However, all the signals, including the generated harmonics, are obtained from the Fourier transform of the induced dipole $\mu(t)$:⁷⁴

$$S(\omega) = \left| \sum_a \int_0^{t_f} dt g(t) [\mu_a(t) - \mu_a^0] e^{-i\omega t} \right|^2, \quad (4)$$

$$g(t) = \begin{cases} e^{-(t-t_s)/\tau}, & \text{for } t \geq t_s, \\ 1, & \text{otherwise,} \end{cases} \quad (5)$$

where the pulse amplitude decays to zero at time t_s , and t_f is the final propagation time. Throughout our analysis, we ensure that the final time t_f ($t_f \approx 200$ fs) is selected such that the dipole amplitude decays to zero for the specified damping parameters.

The linear absorption spectrum is computed from the induced real-time dipole. To access a broad energy range, nanoparticles are subjected to interact with a Dirac delta perturbation in the form of $E_a^\delta(t) = E_{p,a}^\delta \delta(t - t')$, where $E_{p,a}^\delta$ is the field amplitude component for the polarization direction \hat{e}_a , instead of interacting with a laser pulse as used for harmonic signals. For harmonic generation, the purpose of using a pulsed signal is to excite nanoparticles within a well-defined energy range contained within the pulse. This allows for the separation of each harmonic from one another, with harmonics spaced by the driving frequency. This type of calculation can be used to calculate hyper-polarizabilities as described later. From the induced dipole, the polarizability (α_{ab}) component and

absorbance (σ) are computed as

$$\alpha_{ab}(\omega) = \frac{\mu_a^\delta(\omega)}{E_{p,b}^\delta}, \quad (6)$$

$$\sigma(\omega) = \frac{4\pi\omega}{3c} \Im[\alpha_{xx} + \alpha_{yy} + \alpha_{zz}], \quad (7)$$

where $\Im[\cdot]$ denotes the imaginary part of the argument. Here $\mu_a^\delta(\omega)$ is the Fourier transform of the time-dependent dipole $\mu_a^\delta(t)$ which includes damping over time, given by $\mu_a^\delta(\omega) = \int_{-\infty}^{\infty} dt [\mu_a^\delta(t) - \mu_a^0] \times e^{-t/\tau}$.

Polarizability determines absorption, while the first and second hyper-polarizabilities measure the efficiency of SHG and THG for a given particle. All polarizabilities in this paper are calculated according to Eq.6, unless explicitly specified otherwise. However for hyper-polarizabilities, we use a variant on a method developed by Li and co-workers⁶⁸, which involves extracting polarizabilities and hyper-polarizabilities from the real-time dipole. This method allows us to obtain dipole components of different orders, followed by deriving polarizability and hyper-polarizability components through fitting with analytical functions. The Li method works well for nonresonant excitation of small molecules, but for the present case where we have resonant excitation of a plasmonic particle with a large density of states, we find it necessary to modify the method to employ a laser pulse of the form given in Eq.2.

III. RESULTS AND DISCUSSION

A. Systems and Absorption Spectra

1. Systems

Figure 1(a) illustrates the Au nanorod systems used in this study. The symmetry of nanoparticle and polarization direction play important roles for SHG.¹⁶ For a single nanorod, there is symmetry with respect to inversion along the rod axis, but not in the transverse direction (due to the five Au atoms that are around the central axis of the particle, Fig.1(a) side view). As a result, the rod should be inactive for SHG when excited along the rod axis for a linearly polarized laser pulse along that axis, as will be demonstrated later.

To generate asymmetric arrangements of Au atoms along the longitudinal direction, we investigate end-to-end dimer nanorod systems of different lengths as shown in Figure 1. Previous experimental studies of much larger rods have reported the synthesis of end-to-end nanorod systems^{75,76} and investigated nonlinear optical processes using such configurations^{77,78}. In this study, the dimer geometries are generated using previously optimized nanorods. To generate a closed shell configuration, we use a -1 charge for each nanorod system,

resulting in dimer configurations with a total charge of -2. We vary the length of one nanorod system while keeping the length of the other particle unchanged to manipulate the asymmetry i.e. the length ratio between the two particles. Five different length combinations are studied, denoted as Au₇₃-Au_x, with x taking the values 73, 97, 121, 133, and 145. Therefore, we have a symmetric configuration only for $x = 73$ and asymmetric configurations for the rest of the values of x . Here, we use the monomer particle involving 73 atoms (with a length of 3.2 nm) as a reference; however, our findings remain consistent with other particle sizes as references. Different inter nanoparticle spacings ($h=6, 8,$ and 10 Angstroms) are used to modulate interactions between particles. Note that the smallest value chosen is large enough to avoid wavefunction overlap effects that would change the optical response in significant ways. It is worth mentioning that while other dimer geometries (like T-shaped^{79,80}, L-shaped^{80,81}) could alternatively provide spatial asymmetry, for computational simplicity, we restrict this study to the end-to-end dimer configurations.

2. Absorption Spectra

Absorption spectra of the nanorod systems are shown in Figure 1(b, c), as obtained from the real-time calculations through computation of the time-dependent induced dipoles. Additionally, we computed absorption spectra for some systems in the frequency domain using linear response TD-DFTB. The time and frequency domain results agree with each other, providing a validation of the real-time calculations in this study. However, the frequency domain calculations are much more computationally expensive compared to real-time calculations, particularly when a wide energy window and a substantial number of excited states are needed to cover the energy range. Given this, we performed frequency domain computations only for single nanorod geometries (elements of the nanorod dimers) and compared the results with the spectra obtained from real-time calculations, as shown in Fig.1(b).

The dashed vertical lines in Figure 1(b) indicate the maximum absorption peaks, which represent excitation of the longitudinal plasmon mode within each particle. The involved excited states exhibit a collective excitation nature, wherein excitations are characterized as weighted combinations of Kohn-Sham transitions between occupied and virtual molecular orbitals. Transition weights for important excited states near the plasmon energies are listed in the supporting information (SI), Table S1. From the table it is evident that the states consist of several transitions with similar weights. This multi-reference character of the plasmonic excited states has been reported previously.^{82,83}

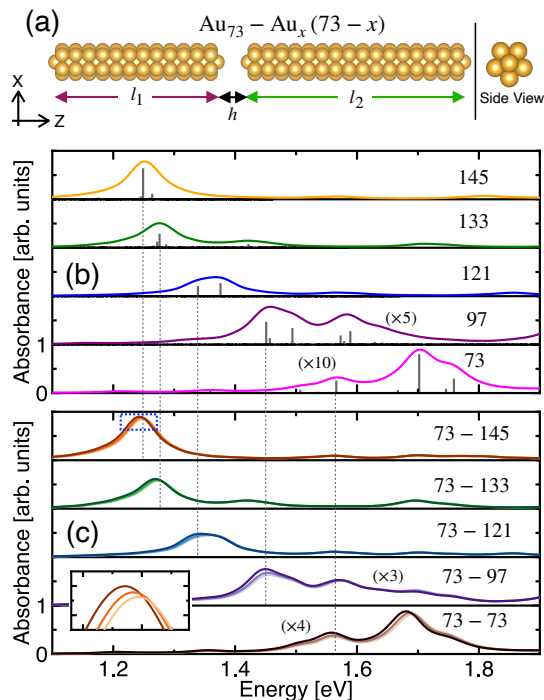


FIG. 1. (a) Nanorod dimer systems used in this study. The two nanoparticles are characterized by lengths l_1 and l_2 respectively, with an inter-spacing of h between them. Absorption spectra for (b) single nanorod and (c) dimer systems. For each system in (c), the inter-particle spacing increases from deep to light color. Spectra are obtained from real-time dipole calculations through Eq.7. In (b), vertical solid lines denote oscillator strengths connecting the ground and excited states through one-photon processes. Spectra are amplified by factors of 10(4) and 5(3) for the 73(73-73) and 97(73-97) systems, respectively, for comparison. The inset in (c) magnifies the peaks for different h values for the 73-145 system within the region indicated by the blue dashed box. Here, the peak intensity of delta kick is $I_p = 1.3 \times 10^7$ W/cm², for calculating the real-time absorption spectra.

The plasmon energy for the individual nanorods shows a noticeable red shift with increasing size of the particle, Fig.1(b), such that for particles consisting of 73, 97, 121, 133, and 145 atoms, the plasmon energies peak at 1.57, 1.45, 1.34, 1.27, and 1.25 eV, respectively. Indeed we find a linear decrease in plasmon energies with particle size as shown in the SI Fig.S1(a). This spectral shift with the nanorod length is consistent with previous experimental⁸⁴⁻⁸⁷ and theoretical^{88,89} studies. Moreover, the absorption amplitude increases with the size of the particle due to the increased transition dipole and density of states accessible for larger particles.

The absorption spectra of the dimer systems are influenced by the individual absorption characteristics of each particle and their interactions. However, the absorption is predominantly influenced by the larger

particles in the dimer structure due to the larger absorption cross-sections compared to the smaller ones, Fig.1(c). The interaction between the particles causes a slight shift in the plasmon energy of the larger particle towards lower energies. This shift becomes more pronounced as the distance between the particles decreases, with the peak shifting by up to 25 meV for an inter-nanoparticle spacing of 6 Å. However, we note that the spectral splitting is smaller when there are significant differences between the plasmon energies of the two particles in the dimer systems. On the other hand, dimers composed of particles of equal length exhibit a larger energy shift, Fig.S1(b). Similar to single nanorod systems, the plasmon peaks show redshift as the length of the particle increases. The plasmon energies for the longitudinal mode of the dimer systems are provided in Table I. The trends in the spectral shifts were also observed in previous studies.⁹⁰⁻⁹³ Furthermore, we observe transverse modes from the XX and YY polarizability components, which appear at relatively higher energies, near 2.05 eV, as depicted in Fig.S5. This mode does not show an energy shift with the nanoparticle length as we maintain a fixed width for the particles.

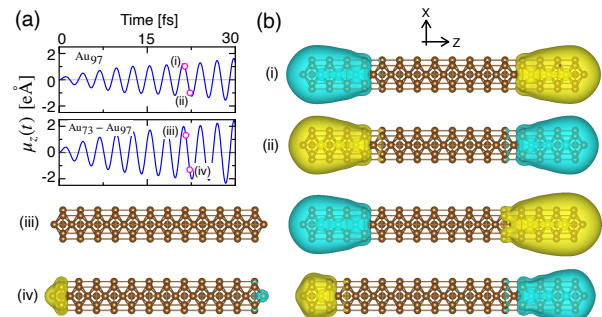


FIG. 2. Snapshots of charge density difference (CDD) for Au_{97} and $Au_{73}-Au_{97}$ systems interacting with a CW laser. (a) Induced dipole and (b) CDD for selected points highlighted in the induced dipole plots. Here, driving frequency $\omega_p = 1.45$ eV, peak intensity $I_p = 1.3 \times 10^7$ W/cm², and polarization direction is along the Z axis. Yellow color represents positive and cyan color represents negative surfaces with equal absolute amplitudes.

In Figure 2, we display the induced dipole and charge oscillation for Au_{97} and $Au_{73}-Au_{97}$ systems interacting with a CW laser of form $E_z(t) = \hat{e}_z E_p \sin(\omega_p t)$. The central frequency of the laser is tuned to match the respective plasmon energies of the particles. The induced dipole for both systems oscillates around their mean values, with its amplitude increasing as more energy is transferred to the systems through interaction with the field over time. We select two points along the time axis representing opposite directions for dipoles but with nearly equal absolute amplitude. For these selected points, charge density difference (CDD) surfaces for both systems are shown in Fig.2(b). The CDD is calculated as

$\Delta q(t) = q(t) - q(0)$, where $q(0)$ is the initial charge density. The surface changes sign when the dipole changes its direction, clearly demonstrating the oscillation of induced charge due to plasmon excitation. Interestingly, the absolute amplitude of the surface is symmetric for the single particle around the center of the nanorod; however, this symmetry is disrupted in dimer geometries in the presence of a second nanoparticle. This asymmetric charge oscillation impacts the SHG process, which we discuss in the following.

B. Second and Third Harmonic Generation (SHG and THG)

In this section, we discuss harmonic generation (HG) processes for nanorod systems and their dependency on pulse parameters and nanoparticle geometries. Signals are obtained following the Eq.4 through the computation of induced dipoles. Here we report signals obtained by integrating dipoles from all possible directions as given in Eq.4, however, the rod structure results are dominated by dipoles along the rod axis. Throughout we use the following laser parameters unless otherwise specified: longitudinal excitation of the plasmon mode achieved by suitably selecting a driving frequency depending on the system, a pulse duration T_p of 14 fs, a filter function (damping) width τ of 30 fs, a laser polarization direction of Z , and an inter-particle spacing h of 6 Å.

1. End-To-End Nanorod Dimer

Figure 3(a) illustrates fundamental dipole (DP), second harmonic generation (SHG), and third harmonic generation (THG) spectra for $\text{Au}_{73}\text{-Au}_{97}$ systems with different gaps h between the particles and a single Au_{97} nanorod. Nonlinear polarization is induced when particles are excited at 1.45 eV, very close to their plasmon energy, through interaction with an intense laser pulse of the form given in Eq.2. For both single and dimer systems, the DP and THG spectra, obtained through the fast Fourier transformation of the induced dipole, peak around their respective energies i.e., around ω_p for DP and $3 \times \omega_p$ for THG. However, only the dimer systems lacking the longitudinal symmetry exhibit activity in SHG around the energy $2 \times \omega_p$, while the single particle provides negligible amplitude for SHG, as clearly evident in Fig.3(a). Further, we refer to the SI, Fig.S2(a), for the comparison of full HG spectra for dimer systems with signals from each nanorod systems. As previously noted, unlike dimer systems of unequal lengths, a single nanorod possesses inversion symmetry along the longitudinal direction and hence remains inactive in SHG.

The first harmonic (DP) spectra contain two major peaks around the central laser frequency as observed in Fig.3(a). These two peaks correspond to excited states

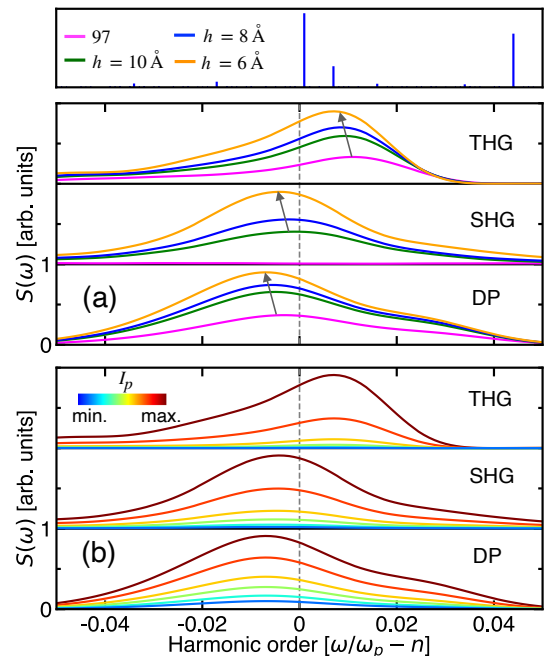


FIG. 3. (a) Fundamental dipole (DP), second harmonic generation (SHG), and third harmonic generation (THG) spectra for single Au_{97} particle and $\text{Au}_{73}\text{-Au}_{97}$ dimers with various inter-particle spacing h . Here, n is the order of the induced optical process, $n = 1, 2,$ and 3 for DP, SHG and THG processes, respectively. In the top row we display oscillator strengths for Au_{97} shifting the energy of each state by ω_p to the lower energy. Here the pump peak intensity is $I_p = 2.5 \times 10^8 \text{ W/cm}^2$, and driving frequency $\omega_p = 1.45 \text{ eV}$. For comparison, all the spectra are normalized to the corresponding spectra of dimer systems for $h = 6$. (b) DP, SHG, and THG spectra for different field intensities. Here, the field intensity increases from 2.3×10^7 to $2.5 \times 10^8 \text{ W/cm}^2$ as indicated by the color gradient from blue to red and $\omega_p = 1.45 \text{ eV}$. The vertical dashed gray line represents the central laser frequency. For comparison, all the spectra are normalized to the corresponding spectra for maximum peak intensity.

with significant oscillator strengths that appear within the energy window of the pump laser as observed in the top row of the figure. The peak position of SHG spectra (only for dimer systems) follows the peaks of DP spectra, while the higher energy peak amplitude is significantly suppressed compared to the DP spectra. However, THG spectra show maxima at higher energy that is in between the two peaks in the DP results, which is suggestive of combination mode excitation. Overall, the spectrum gets narrower as we move to higher order processes from DP to THG as the higher order processes are more sensitive to the resonant driving field.

Moreover, the DP spectra in Fig.3(a) show a slight red-shift with increased peak amplitudes as h decreases, a trend consistent with the red-shift observed in the linear absorption spectrum, as shown in Fig.1(c). Interestingly, both SHG and THG spectra also follow a similar energy

shift towards lower energies with decreasing h . The spectral shifts in the SHG and THG spectra are comparable to the shift of the dipole spectra. Additionally, the amplitudes of the nonlinear signals increase similarly to the DP response but at a higher rate, as depicted in Fig.S2(b). Similar enhancements in SHG⁹⁴ and THG^{78,95} results for smaller inter-particle spacings have also been reported in experiments.

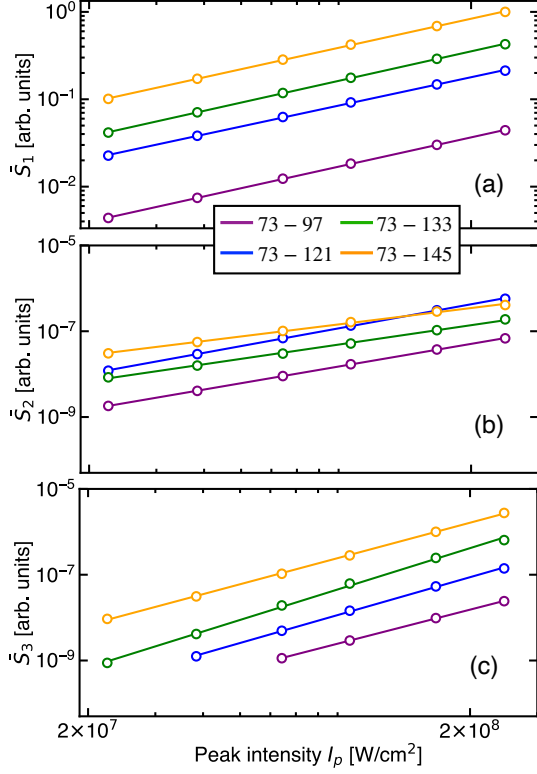


FIG. 4. Integrated (a) DP, (b) SHG, and (c) THG signals as a function of pump intensity for all dimer systems used in this study. All the signal amplitudes are normalized by a constant factor for comparison.

TABLE I. Length ratio, LSPR energy, and exponents for power scaling of the DP, SHG, and THG processes as a function pump intensity for dimer systems.

System	Length Ratio (l_2/l_1)	LSPR [eV]	DP	SHG	THG
73-97	1.33	1.45	0.97	1.52	2.29
73-121	1.66	1.34	0.94	1.62	2.54
73-133	1.83	1.27	0.97	1.3	2.78
73-145	2	1.24	0.96	1.1	2.38

2. Pump Intensity

The DP and HG spectra for different pump intensities for the Au₇₃-Au₉₇ system are shown in Fig.3(b). The

overall amplitude for all spectra increases with the field intensity as a higher photon density induces a larger polarization within the nanorod systems. Importantly, despite the increase in amplitude, the shape of the spectra remains largely unchanged across all the intensities. This highlights the stability of the process under varying pump intensities.

The scaling of the DP and HG signals as a function of pump intensity for all the dimer systems is shown in Fig.4. Here, we use integrated spectra for the yield of the signals as $\bar{S}_n = \int_{\Delta\omega_{n-}}^{\Delta\omega_{n+}} d\omega S(\omega)$, where $\Delta\omega_n$ is the energy window around the center of the n -th order signal. Throughout this paper, we maintain a consistent energy window size, defined as $\Delta\omega_{n\pm} = (n \pm 0.05) \times \omega_p$.

The comparison of signal yield for different pump intensities reveals significant differences among the various HG processes. As observed in the Fig.4, all the signals follow the power law dependency, expressed as $\bar{S}_n \propto I_p^n$, with pump intensity I_p . The slopes obtained from linear fits represent the power dependence of the respective processes on the incident field intensity. All the slopes, along with their respective plasmon energies, are listed in Table I. As is evident from the table, the DP signals depend of the pump intensity almost linearly with an exponent between 0.94 – 1 as expected. On the other hand, the slopes for the SHG signals range between 1.1 and 1.6, while those for the THG signals are between 2.3 and 2.8. This observation reflects the nonlinearity in SHG and THG compared to the DP signals. Moreover, the deviation of the HG exponents from the perturbative results ($n = 2$ for SHG and $n = 3$ for THG) indicate a saturation phenomenon, signifying the non-perturbative characteristics of HG under intense laser pulses. Deviation from the perturbative results for the lower-order harmonics (SHG and THG) has been noted in previous works.^{96–98} Specifically, exponents for the power law dependencies on-field intensity were found to be smaller than those predicted by perturbation theory. Furthermore, we note contributions from the overlap between the dominant dipole and HG signals, leading to significantly smaller SHG and THG exponents. This effect is particularly pronounced for larger dimer systems, where the amplitudes of the DP signals are substantially larger.

Detectable HG signals are observed only when the nanorod systems interact with intense laser fields, while dipole modes at the fundamental frequency can be excited at relatively weak field intensities. As a result, the amplitudes of the dipole signals are significantly larger than those of the HG by several orders of magnitude, as observed in Fig.4(a). Indeed, the amplitudes of SHG and THG signals are comparable within the same orders of magnitude. Particularly, SHG signals exhibit larger amplitudes at lower intensities compared to THG signals, while THG signals become dominant at higher intensities, given their higher sensitivity to field

intensities.

The amplitudes of DP and THG signals increase with increasing nanorod lengths from 73-97 to 73-145, Fig.4(a, c). A similar trend is also observed for SHG except for the 73-121 system, which has a higher SHG yield for an intermediate length. One possible reason for this dependence could be the presence of a larger number of states with significant oscillator strength that are near the plasmon energy (Fig. 1(b, c)) than occurs for the other nanorods, which serves to amplify the SHG signal. This effect does not extend to the DP and THG results, so asymmetry in the excited states is also a factor. We note experimental studies that have reported an increase in the SHG^{99,100} and THG³⁷ yields with the increasing nanoparticle size. Our results show a similar trend, particularly for larger particles, where the oscillator strengths for plasmon-excited states dominate significantly over other contributing states that may overlap with plasmon excitation. For nanorods, one experiment shows an increase in SHG with an increasing aspect ratio⁹⁹ while another shows a decrease¹⁰⁰. This is related to the variations with length that we see in Fig. 1(b))

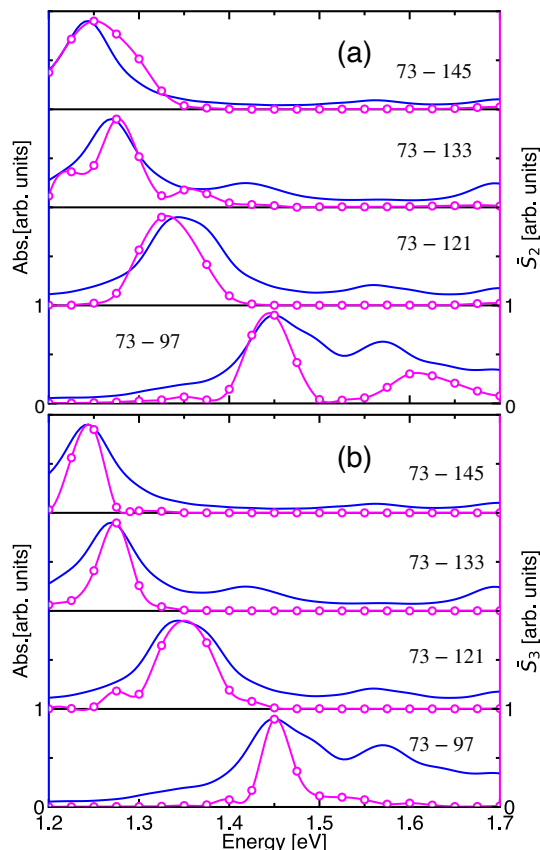


FIG. 5. Pump frequency dependent (a) SHG and (b) THG signals. HG signals are compared with the corresponding linear absorption spectra. For comparison, peak amplitudes for all the spectra are normalized. Here, $I_p = 9.7 \times 10^7$ W/cm².

3. Pump Frequency

Figure 5 displays SHG and THG signals as a function of pump frequency (i.e., action spectra) for all the dimer systems used in this study. As discussed earlier, the LSPR energy undergoes a significant red shift with increasing rod length. As a result, analyzing how incident frequency affects HG processes by changing the particle length and hence modifying the LSPR energy reveals the important role of plasmon resonance in HG efficiency.

Irrespective of the nanorod lengths, both SHG and THG signals are similar to the linear absorption spectrum of the nanorod systems, Fig.5. However, the HG signals are significantly suppressed outside a region with a width ~ 0.1 eV that corresponds to LSPR excitation. Although smaller transitions exist in the linear spectra outside this LSPR energy range, these smaller absorption amplitudes are not effective in inducing the nonlinear processes. This clearly demonstrates the role of the LSPR in HG processes. Previous studies (both theory and experiment) have reported a similar frequency dependence for both SHG and THG processes where the nonlinear responses closely follow plasmon excitation.^{9,101-103}

Furthermore, the THG signals exhibit narrower profiles compared to SHG signals. Interestingly, we observe that the THG maxima align closer with the linear absorption spectra peaks compared to SHG. This difference between THG and SHG can be attributed to the higher sensitivity of THG to the incident field amplitude relative to SHG.

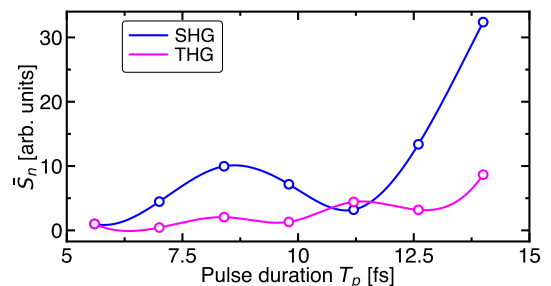


FIG. 6. Integrated SHG and THG signals as a function of pulse duration T_p for Au₇₃-Au₉₇ systems. For comparison, all signals are normalized to 1 for the smallest T_p value. Here, $I_p = 9.7 \times 10^7$ W/cm².

4. Pump Duration

The dependence of HG signals on laser pulse duration T_p is shown in the Figure 6. This study explores how variations in the temporal characteristics of the laser pulse influence the induced signals, providing insights

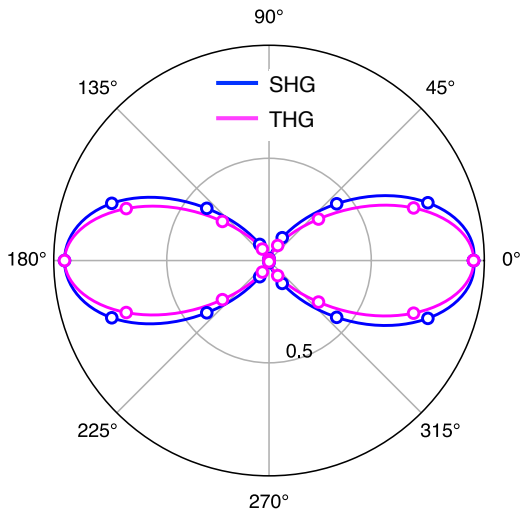


FIG. 7. Integrated SHG and THG signals as a function of pump laser polarization direction for $\text{Au}_{73}\text{-Au}_{97}$ system, making an angle θ with respect to the Z axis in the $X-Z$ plane. Here, $\theta = 0^\circ$ signifies alignment of the laser polarization with the Z axis and $I_p = 9.7 \times 10^7 \text{ W/cm}^2$. The peak amplitudes ($\theta = 0^\circ$) for both SHG and THG are normalized to 1.

into the intricate dynamics of the nonlinear optical processes under consideration.

Pulse duration is changed in such a way that the energy content of the pulse remains unchanged, i.e. $\int_{-\infty}^{\infty} dt E^2(t) = \text{Constant}$. Therefore, the peak intensity of the pulse decreases as T_p increases. We note that the pulse always starts at $t = 0$ and hence the center of the pulse shifts to larger values with the increase of T_p .

Interestingly, the overall amplitude for both SHG and THG signals tends to increase on average (with oscillations) with the increase in T_p , and the SHG amplitude rises rapidly above 12 fs. The increase suggests that longer pulses, for which there is dephasing of the electronic states while they are being excited are more efficient for harmonic generation. This can result because the dephased states have higher oscillator strength. The results in Figure 6 are consistent with previous experiments where several detectable harmonics are observed for long pulse durations but were not observed for short pulse durations.⁹⁷

5. Pump Polarization

Laser polarization dependent HG signals for $\text{Au}_{73}\text{-Au}_{97}$ systems are shown in Figure 7. As seen in the figure, maximum yield is obtained when the laser polarization aligns with the longitudinal axis of the nanorod systems. Both SHG and THG amplitudes decrease as the polarization angle changes from the longitudinal alignment.

This observation again confirms that resonant excitation of plasmon modes leads to efficient HG processes. A similar polarization dependence for SHG has also been reported previously for nanorod systems¹⁰⁴ as well as for nanosphere dimer systems⁹⁴. However, THG amplitude decreases more rapidly compared to SHG due to its higher sensitivity to the laser pulse.

We do not observe significant amplitudes for perpendicular alignment of laser polarization with the longitudinal axis, even when changing the pump energy up to 2.05 eV, where the transverse mode peak appears. However, the XX and YY polarizability components are significantly smaller than the ZZ component near the transverse energy, Table II and Fig.S5. This is because the nanorod is significantly narrower and contains only a few atoms along the transverse direction for the systems we studied here.

TABLE II. Imaginary part of XX , YY , and ZZ components for α , ZZZ component for β , and $ZZZZ$ for γ . The results are obtained near the respective longitudinal plasmon peak energies for ZZ component of α , ZZZ component of β , and $ZZZZ$ component of γ . For the remaining α components, they are evaluated around the transverse plasmon energy. α values are obtained through Eq.6, while β and γ are obtained through dipole fitting following the work by Li and co-workers⁶⁸.

Systems	α [cm^3]			β_{zzz} [10^{-26} esu]	γ_{zzzz} [10^{10} a.u.]
	α_{xx} [10^{-22}]	α_{yy} [10^{-22}]	α_{zz} [10^{-20}]		
73-97	1.29	1.29	2.34	2.1	-
73-121	1.47	1.47	4.89	2.2	8
73-133	1.51	1.51	5.94	3.2	141.3
73-145	1.75	1.75	9.76	3	256.5

6. (Hyper-)Polarizability Calculations

To quantify our study of nonlinear optical properties, we have extracted the polarizability (α), first hyper-polarizability (β), and second hyper-polarizability (γ). Table II presents the XX , YY , and ZZ components of α , ZZZ component of β , and $ZZZZ$ component of γ . While polarizabilities are obtained through Eq.6, hyper-polarizabilities are obtained from dipole fitting following the method introduced by Li and co-workers⁶⁸. Furthermore, we computed polarizabilities in the frequency domain by evaluating excited states and transition dipoles between ground and excited states. These results exhibit agreement with each other for both peak positions and amplitudes, as shown in Fig.S4. Note that we only provide ZZZ and $ZZZZ$ components for β and γ , respectively, as the transverse

excitation is negligibly small for the HG signals for the systems we consider. For the ZZ , ZZZ , and $ZZZZ$ components, results are provided at the respective plasmon energies of the longitudinal mode. On the other hand, the results for the XX and YY components of α are provided at the transverse plasmon energy of 2.05 eV.

We note that because of the high density of electronic states that are close to resonance with the driving field, a different pulse shape for the driving field is employed in this study compared to the form used in the study by Li and co-workers⁶⁸. The use of Eq.2 involves a more gradual increase in the driving field than the linear ramp over one optical period that was used by Li and co-workers. For comparison of our method with reported results by Li and co-workers, we studied the same molecule, para-nitroaniline, and the resulting (hyper-)polarizabilities are given in Table S2. The fitting performance for that molecule and for one of the nanoparticles we studied is illustrated in Fig.S6. Overall the agreement with Li and colleagues is quite good.

As observed in Table II, both polarizability and hyper-polarizabilities increase with size of the system. Furthermore, our findings are consistent with reported linear absorption results that utilize the TD-DFTB method for icosahedral Ag and Au nanoparticles,¹⁰⁵ with absorption cross sections in the range of 10^{-15} to 10^{-14} cm² for both their results and ours. However, it is also important to note that the polarizability results are sensitive to the choice of damping rate. While Douglas-Gallardo et al.¹⁰⁵ employed a damping time of 7 fs, we find that for this choice of damping time, polarizabilities are nearly a factor of 2 smaller than what we obtain for 20 fs, as shown in Fig.S3.

Concerning the first hyper-polarizabilities, Ngo et al.¹⁰⁰ reported measured β values for nanosphere and nanorod systems with sphere diameters down to 3 nm, and the results for the smallest particles are similar in magnitude 10^{-26} – 10^{-25} esu to our results. We also note that there have been previous calculations of static hyper-polarizabilities using TDDFT for gold clusters, and the results are much smaller, 10^{-29} esu, as expected.¹⁰⁶

For the second hyper-polarizabilities, although there have been several reported THG measurements for gold nanoparticles (usually as films) as has been reviewed,¹⁰⁷ we are not aware that values of γ have been reported. The values we report, roughly 10^{12} atomic units, or 5×10^{-28} esu, are larger about a factor of 10^3 than the largest values tabulated for optimized organic oligomers.¹⁰⁸ This seems reasonable given that we are calculating the resonant response rather than the nonresonant response that was considered for the organic molecules.

IV. CONCLUSIONS

In conclusion, this study investigates the dependence of laser pulse parameters on nonlinear optical processes, particularly second and third harmonic generation, for end-to-end Au nanorod dimer systems for variable length ratios and inter-particle spacing. All harmonic generation (HG) signals are derived from induced dipoles for nanorod systems interacting with external laser pulses computed using the real-time time-dependent density functional tight-binding (RT-TDDFTB) method. The characteristics of the obtained HG signals align with previously reported results based on TD-DFT, but the calculations are orders of magnitude faster, which means we can study much larger structures.

Detectable second harmonic generation (SHG) signals are observed only in nanorod dimer systems with broken longitudinal symmetry due to different length ratios. The HG yield increases with the particle size, and a smaller inter-particle spacing is found to be more effective for these processes to occur. The intensity dependence of all generated signals follows a power law in the electric field intensity, with exponents comparable to perturbative results, although higher order harmonics involve non-perturbative contributions. The study of HG yield as a function of incident frequency and laser polarization highlights the significance of resonant excitation of plasmon modes for efficient HG processes. Longer pulse durations are identified as producing more efficient nonlinear excitation for a fixed energy per pulse. Finally, we report the polarizability and first and second hyper-polarizability components for the dimer systems. These are computed from the induced real-time dipoles using a Dirac delta excitation for the polarizabilities and using pulsed excitation for the hyper-polarizabilities. The calculated first hyper-polarizability compares well with a measured result for a small gold nanorod.

Overall, these findings highlight the use of the RT-TDDFTB method in elucidating the role of laser parameters and nanorod characteristics in governing nonlinear optical processes. This study provides valuable insights for the design and optimization of nanoscale optical devices.

ACKNOWLEDGMENTS

This research was supported by the Office of Basic Energy Science, Department of Energy, through grant DE-SC0004752.

REFERENCES

- S.-P. Tai, Y. Wu, D.-B. Shieh, L.-J. Chen, K.-J. Lin, C.-H. Yu, S.-W. Chu, C.-H. Chang, X.-Y. Shi, Y.-C. Wen, K.-H. Lin, T.-

- M. Liu, and C.-K. Sun, "Molecular imaging of cancer cells using plasmon-resonant-enhanced third-harmonic-generation in silver nanoparticles," *Adv. Mater.* **19**, 4520–4523 (2007).
- ²P. Pantazis, J. Maloney, D. Wu, and S. E. Fraser, "Second harmonic generating (shg) nanopores for in vivo imaging," *Proc. Natl. Acad. Sci. (U. S. A.)* **107**, 14535–14540 (2010).
- ³X. Mi, Y. Wang, R. Li, M. Sun, Z. Zhang, and H. Zheng, "Multiple surface plasmon resonances enhanced nonlinear optical microscopy," *Nanophotonics* **8**, 487–493 (2019).
- ⁴Q. Bao and K. P. Loh, "Graphene photonics, plasmonics, and broadband optoelectronic devices," *ACS Nano* **6**, 3677–3694 (2012).
- ⁵Y. Li, N. An, Z. Lu, Y. Wang, B. Chang, T. Tan, X. Guo, X. Xu, J. He, H. Xia, Z. Wu, Y. Su, Y. Liu, Y. Rao, G. Soavi, and B. Yao, "Nonlinear co-generation of graphene plasmons for optoelectronic logic operations," *Nat. Commun.* **13** (2022), 10.1038/s41467-022-30901-8.
- ⁶P. J. Campagnola and L. M. Loew, "Second-harmonic imaging microscopy for visualizing biomolecular arrays in cells, tissues and organisms," *Nat. Biotechnol.* **21**, 1356–1360 (2003).
- ⁷W. P. Dempsey, S. E. Fraser, and P. Pantazis, "Shg nanopores: Advancing harmonic imaging in biology," *BioEssays* **34**, 351–360 (2012).
- ⁸G. Deka, C.-K. Sun, K. Fujita, and S.-W. Chu, "Nonlinear plasmonic imaging techniques and their biological applications," *Nanophotonics* **6**, 31–49 (2017).
- ⁹R. C. Johnson, J. Li, J. T. Hupp, and G. C. Schatz, "Hyper-rayleigh scattering studies of silver, copper, and platinum nanoparticle suspensions," *Chem. Phys. Lett.* **356**, 534–540 (2002).
- ¹⁰E. C. Hao, G. C. Schatz, R. C. Johnson, and J. T. Hupp, "Hyper-rayleigh scattering from silver nanoparticles," *J. Chem. Phys.* **117**, 5963–5966 (2002).
- ¹¹S. Kim, J. Jin, Y.-J. Kim, I.-Y. Park, Y. Kim, and S.-W. Kim, "High-harmonic generation by resonant plasmon field enhancement," *Nature* **453**, 757–760 (2008).
- ¹²M. Kauranen and A. V. Zayats, "Nonlinear plasmonics," *Nat. Photonics* **6**, 737–748 (2012).
- ¹³L. Bonacina, P.-F. Brevet, M. Finazzi, and M. Celebrano, "Harmonic generation at the nanoscale," *J. Appl. Phys.* **127**, 230901 (2020).
- ¹⁴J. Schust, F. Mangold, F. Sterl, N. Metz, T. Schumacher, M. Lippitz, M. Hentschel, and H. Giessen, "Spatially resolved nonlinear plasmonics," *Nano Lett.* **23**, 5141–5147 (2023).
- ¹⁵P. A. Franken, A. E. Hill, C. W. Peters, and G. Weinreich, "Generation of optical harmonics," *Phys. Rev. Lett.* **7**, 118–119 (1961).
- ¹⁶J. A. Armstrong, N. Bloembergen, J. Ducuing, and P. S. Pershan, "Interactions between light waves in a nonlinear dielectric," *Phys. Rev.* **127**, 1918–1939 (1962).
- ¹⁷K. Miyazaki and H. Sakai, "High-order harmonic generation in rare gases with intense subpicosecond dye laser pulses," *J. Phys. B: At. Mol. Opt. Phys.* **25**, L83 (1992).
- ¹⁸A. L'Huillier and P. Balcou, "High-order harmonic generation in rare gases with a 1-ps 1053-nm laser," *Phys. Rev. Lett.* **70**, 774–777 (1993).
- ¹⁹J. J. Macklin, J. D. Kmetec, and C. L. Gordon, "High-order harmonic generation using intense femtosecond pulses," *Phys. Rev. Lett.* **70**, 766–769 (1993).
- ²⁰Y. Liang, S. Augst, S. L. Chin, Y. Beaudoin, and M. Chaker, "High harmonic generation in atomic and diatomic molecular gases using intense picosecond laser pulses—a comparison," *J. Phys. B: At. Mol. Opt. Phys.* **27**, 5119 (1994).
- ²¹C. Lynga, A. L'Huillier, and C.-G. Wahlstrom, "High-order harmonic generation in molecular gases," *J. Phys. B: At. Mol. Opt. Phys.* **29**, 3293 (1996).
- ²²T. T. Luu, Z. Yin, A. Jain, T. Gaumnitz, Y. Pertot, J. Ma, and H. J. Wörner, "Extreme-ultraviolet high-harmonic generation in liquids," *Nat. Commun.* **9** (2018), 10.1038/s41467-018-06040-4.
- ²³S. Ghimire and D. A. Reis, "High-harmonic generation from solids," *Nat. Phys.* **15**, 10–16 (2019).
- ²⁴K. Koshelev, S. Kruk, E. Melik-Gaykazyan, J.-H. Choi, A. Bogdanov, H.-G. Park, and Y. Kivshar, "Subwavelength dielectric resonators for nonlinear nanophotonics," *Science* **367**, 288–292 (2020).
- ²⁵J. Butet, P.-F. Brevet, and O. J. F. Martin, "Optical second harmonic generation in plasmonic nanostructures: From fundamental principles to advanced applications," *ACS Nano* **9**, 10545–10562 (2015).
- ²⁶C.-C. Zhang, J.-Y. Zhang, J.-R. Feng, S.-T. Liu, S.-J. Ding, L. Ma, and Q.-Q. Wang, "Plasmon-enhanced second harmonic generation of metal nanostructures," *Nanoscale* **16**, 5960–5975 (2024).
- ²⁷J. Nappa, G. Revillod, I. Russier-Antoine, E. Benichou, C. Jonin, and P. F. Brevet, "Electric dipole origin of the second harmonic generation of small metallic particles," *Phys. Rev. B* **71**, 165407 (2005).
- ²⁸K. A. Willets and R. P. Van Duyne, "Localized surface plasmon resonance spectroscopy and sensing," *Annu. Rev. Phys. Chem.* **58**, 267–297 (2007).
- ²⁹K. L. Kelly, E. Coronado, L. L. Zhao, and G. C. Schatz, "The optical properties of metal nanoparticles: The influence of size, shape, and dielectric environment," *J. Phys. Chem. B* **107**, 668–677 (2003).
- ³⁰C. K. Chen, A. R. B. de Castro, and Y. R. Shen, "Surface-enhanced second-harmonic generation," *Phys. Rev. Lett.* **46**, 145–148 (1981).
- ³¹T. Hanke, G. Krauss, D. Träutlein, B. Wild, R. Bratschitsch, and A. Leitenstorfer, "Efficient nonlinear light emission of single gold optical antennas driven by few-cycle near-infrared pulses," *Phys. Rev. Lett.* **103**, 257404 (2009).
- ³²J. Butet, J. Duboisset, G. Bachelier, I. Russier-Antoine, E. Benichou, C. Jonin, and P.-F. Brevet, "Optical second harmonic generation of single metallic nanoparticles embedded in a homogeneous medium," *Nano Lett.* **10**, 1717–1721 (2010).
- ³³L.-J. Black, P. R. Wiecha, Y. Wang, C. H. de Groot, V. Paillard, C. Girard, O. L. Muskens, and A. Arbouet, "Tailoring second-harmonic generation in single l-shaped plasmonic nanoantennas from the capacitive to conductive coupling regime," *ACS Photonics* **2**, 1592–1601 (2015).
- ³⁴B. Metzger, L. Gui, J. Fuchs, D. Floess, M. Hentschel, and H. Giessen, "Strong enhancement of second harmonic emission by plasmonic resonances at the second harmonic wavelength," *Nano Lett.* **15**, 3917–3922 (2015).
- ³⁵A. Noor, A. R. Damodaran, I.-H. Lee, S. A. Maier, S.-H. Oh, and C. Ciraci, "Mode-matching enhancement of second-harmonic generation with plasmonic nanopatch antennas," *ACS Photonics* **7**, 3333–3340 (2020).
- ³⁶Q. Ai, F. Sterl, H. Zhang, J. Wang, and H. Giessen, "Giant second harmonic generation enhancement in a high-q doubly resonant hybrid plasmon–fiber cavity system," *ACS Nano* **15**, 19409–19417 (2021).
- ³⁷M. Lippitz, M. A. van Dijk, and M. Orrit, "Third-harmonic generation from single gold nanoparticles," *Nano Lett.* **5**, 799–802 (2005).
- ³⁸T. Shibanuma, G. Grinblat, P. Albella, and S. A. Maier, "Efficient third harmonic generation from metal–dielectric hybrid nanoantennas," *Nano Lett.* **17**, 2647–2651 (2017).
- ³⁹M. Sukharev and R. Pachter, "Effects of exciton–plasmon strong coupling on third harmonic generation by two-dimensional WS₂ at periodic plasmonic interfaces," *J. Chem. Phys.* **148**, 094701 (2018).
- ⁴⁰A. C. R. Pipino, G. C. Schatz, and R. P. Van Duyne, "Surface-enhanced second-harmonic diffraction: Selective enhancement by spatial harmonics," *Phys. Rev. B* **49**, 8320–8330 (1994).
- ⁴¹H. Chen, J. M. McMahon, M. A. Ratner, and G. C. Schatz, "Classical electrodynamics coupled to quantum mechanics for calculation of molecular optical properties: a rt-tddft/fdtd approach," *J. Phys. Chem. C* **114**, 14384–14392 (2010).

- ⁴²H. Chen, M. G. Blaber, S. D. Standridge, E. J. DeMarco, J. T. Hupp, M. A. Ratner, and G. C. Schatz, "Computational modeling of plasmon-enhanced light absorption in a multicomponent dye sensitized solar cell," *J. Phys. Chem. C* **116**, 10215–10221 (2012).
- ⁴³Y. Gao and D. Neuhauser, "Dynamical quantum-electrodynamics embedding: Combining time-dependent density functional theory and the near-field method," *J. Chem. Phys.* **137**, 074113 (2012).
- ⁴⁴L. Zhao, L. Jensen, and G. C. Schatz, "Pyridine-ag₂₀ cluster: A model system for studying surface-enhanced raman scattering," *J. Am. Chem. Soc.* **128**, 2911–2919 (2006).
- ⁴⁵C. M. Aikens and G. C. Schatz, "Tddft studies of absorption and sers spectra of pyridine interacting with au₂₀," *J. Phys. Chem. A* **110**, 13317–13324 (2006).
- ⁴⁶D. Marinica, A. Kazansky, P. Nordlander, J. Aizpurua, and A. G. Borisov, "Quantum plasmonics: Nonlinear effects in the field enhancement of a plasmonic nanoparticle dimer," *Nano Lett.* **12**, 1333–1339 (2012).
- ⁴⁷G. Aguirregabiria, D. C. Marinica, R. Esteban, A. K. Kazansky, J. Aizpurua, and A. G. Borisov, "Electric field-induced high order nonlinearity in plasmonic nanoparticles retrieved with time-dependent density functional theory," *ACS Photonics* **4**, 613–620 (2017).
- ⁴⁸A. Babaze, R. Esteban, J. Aizpurua, and A. G. Borisov, "Second-harmonic generation from a quantum emitter coupled to a metallic nanoantenna," *ACS Photonics* **7**, 701–713 (2020).
- ⁴⁹R. L. Gieseck, M. A. Ratner, and G. C. Schatz, "Semiempirical modeling of ag nanoclusters: New parameters for optical property studies enable determination of double excitation contributions to plasmonic excitation," *J. Phys. Chem. A* **120**, 4542–4549 (2016).
- ⁵⁰R. L. Gieseck, M. A. Ratner, and G. C. Schatz, "Theoretical modeling of voltage effects and the chemical mechanism in surface-enhanced raman scattering," *Faraday Discuss.* **205**, 149–171 (2017).
- ⁵¹K. Lopata and D. Neuhauser, "Nonlinear nanopolaritonics: Finite-difference time-domain Maxwell–Schrödinger simulation of molecule-assisted plasmon transfer," *J. Chem. Phys.* **131**, 014701 (2009).
- ⁵²J. Zhou, M. Hu, Y. Zhang, P. Zhang, W. Liu, and S. Liu, "Numerical analysis of electron-induced surface plasmon excitation using the fdtd method," *J. Opt.* **13**, 035003 (2011).
- ⁵³M. Sukharev, "Finite-difference time-domain technique," in *Encyclopedia of Nanotechnology* (Springer Netherlands, 2016) pp. 1207–1216.
- ⁵⁴M. Sukharev and A. Nitzan, "Optics of exciton-plasmon nanomaterials," *J. Phys.: Condens. Matter* **29**, 443003 (2017).
- ⁵⁵A. Amirjani and S. K. Sadrezaad, "Computational electromagnetics in plasmonic nanostructures," *J. Mater. Chem. C* **9**, 9791–9819 (2021).
- ⁵⁶S. A. Shah, M. R. Clark, J. Zyss, M. Sukharev, and A. Piryatinski, "Interplay between gain and loss in arrays of nonlinear plasmonic nanoparticles: toward parametric downconversion and amplification," *Opt. Lett.* **49**, 1680–1683 (2024).
- ⁵⁷B. Hourahine, B. Aradi, V. Blum, F. Bonafé, A. Buccheri, C. Camacho, C. Cevallos, M. Y. Deshayé, T. Dumitrică, A. Dominguez, S. Ehlert, M. Elstner, T. van der Heide, J. Hermann, S. Irle, J. J. Kranz, C. Köhler, T. Kowalczyk, T. Kubař, I. S. Lee, V. Lutsker, R. J. Maurer, S. K. Min, I. Mitchell, C. Negre, T. A. Niehaus, A. M. N. Niklasson, A. J. Page, A. Pecchia, G. Penazzi, M. P. Persson, J. Řezáč, C. G. Sánchez, M. Sternberg, M. Stöhr, F. Stuckenberg, A. Tkatchenko, V. W.-z. Yu, and T. Frauenheim, "DFTB+, a software package for efficient approximate density functional theory based atomistic simulations," *J. Chem. Phys.* **152**, 124101 (2020).
- ⁵⁸F. P. Bonafé, B. Aradi, B. Hourahine, C. R. Medrano, F. J. Hernández, T. Frauenheim, and C. G. Sánchez, "A real-time time-dependent density functional tight-binding implementation for semiclassical excited state electron–nuclear dynamics and pump–probe spectroscopy simulations," *J. Chem. Theory Comput.* **16**, 4454–4469 (2020).
- ⁵⁹S. I. Allec, Y. Sun, J. Sun, C.-e. A. Chang, and B. M. Wong, "Heterogeneous cpu+gpu-enabled simulations for dftb molecular dynamics of large chemical and biological systems," *J. Chem. Theory Comput.* **15**, 2807–2815 (2019).
- ⁶⁰M. Van den Bossche, "Dftb-assisted global structure optimization of 13- and 55-atom late transition metal clusters," *J. Phys. Chem. A* **123**, 3038–3045 (2019).
- ⁶¹N. Asadi-Aghbolaghi, R. Rüger, Z. Jamshidi, and L. Visscher, "Td-dft+tb: An efficient and fast approach for quantum plasmonic excitations," *J. Phys. Chem. C* **124**, 7946–7955 (2020).
- ⁶²S. D'Agostino, R. Rinaldi, G. Cuniberti, and F. Della Sala, "Density functional tight binding for quantum plasmonics," *J. Phys. Chem. C* **122**, 19756–19766 (2018).
- ⁶³S. K. Giri and G. C. Schatz, "Photodissociation of h₂ on ag and au nanoparticles: Effect of size and plasmon versus interband transitions on threshold intensities for dissociation," *J. Phys. Chem. C* **127**, 4115–4123 (2023).
- ⁶⁴S. K. Giri and G. C. Schatz, "Plasmon enhanced spectroscopy and photocatalysis," arXiv:2402.13478 (2024), <https://doi.org/10.48550/arXiv.2402.13478>.
- ⁶⁵G. Jha and T. Heine, "Dftb parameters for the periodic table: Part iii, spin-orbit coupling," *J. Chem. Theory Comput.* **18**, 4472–4481 (2022).
- ⁶⁶O. A. Douglas-Gallardo, M. Berdakin, and C. G. Sánchez, "Atomistic insights into chemical interface damping of surface plasmon excitations in silver nanoclusters," *J. Phys. Chem. C* **120**, 24389–24399 (2016).
- ⁶⁷C. Mansilla Wettstein, F. P. Bonafé, M. B. Oviedo, and C. G. Sánchez, "Optical properties of graphene nanoflakes: Shape matters," *J. Chem. Phys.* **144**, 224305 (2016).
- ⁶⁸F. Ding, B. E. Van Kuiken, B. E. Eichinger, and X. Li, "An efficient method for calculating dynamical hyperpolarizabilities using real-time time-dependent density functional theory," *J. Chem. Phys.* **138**, 064104 (2013).
- ⁶⁹T. P. Rossi, P. Erhart, and M. Kuisma, "Hot-carrier generation in plasmonic nanoparticles: The importance of atomic structure," *ACS Nano* **14**, 9963–9971 (2020).
- ⁷⁰E. J. Zeman and G. C. Schatz, "An accurate electromagnetic theory study of surface enhancement factors for silver, gold, copper, lithium, sodium, aluminum, gallium, indium, zinc, and cadmium," *J. Chem. Phys.* **91**, 634–643 (1987).
- ⁷¹M. G. Blaber, M. D. Arnold, and M. J. Ford, "Search for the ideal plasmonic nanoshell: The effects of surface scattering and alternatives to gold and silver," *J. Phys. Chem. C* **113**, 3041–3045 (2009).
- ⁷²A. L. Schmucker, N. Harris, M. J. Banholzer, M. G. Blaber, K. D. Osberg, G. C. Schatz, and C. A. Mirkin, "Correlating nanorod structure with experimentally measured and theoretically predicted surface plasmon resonance," *ACS Nano* **4**, 5453–5463 (2010).
- ⁷³A. L. Schmucker, N. Harris, M. J. Banholzer, M. G. Blaber, K. D. Osberg, G. C. Schatz, and C. A. Mirkin, "Correction to correlating nanorod structure with experimentally measured and theoretically predicted surface plasmon resonance," *ACS Nano* **5**, 7685–7685 (2011).
- ⁷⁴E. Coccia and E. Luppi, "Time-dependent ab initio approaches for high-harmonic generation spectroscopy," *J. Phys.: Condens. Matter* **34**, 073001 (2021).
- ⁷⁵K. K. Caswell, J. N. Wilson, U. H. F. Bunz, and C. J. Murphy, "Preferential end-to-end assembly of gold nanorods by biotin-streptavidin connectors," *J. Am. Chem. Soc.* **125**, 13914–13915 (2003).
- ⁷⁶X. Lu, D. Punj, and M. Orrit, "Controlled synthesis of gold nanorod dimers with end-to-end configurations," *RSC Adv.* **12**, 13464–13471 (2022).
- ⁷⁷T. Hanke, G. Krauss, D. Träutlein, B. Wild, R. Bratschitsch, and A. Leitenstorfer, "Efficient nonlinear light emission of single gold optical antennas driven by few-cycle near-infrared pulses,"

- Phys. Rev. Lett. **103**, 257404 (2009).
- ⁷⁸H. Harutyunyan, G. Volpe, R. Quidant, and L. Novotny, “Enhancing the nonlinear optical response using multifrequency gold-nanowire antennas,” Phys. Rev. Lett. **108**, 217403 (2012).
- ⁷⁹B. K. Canfield, H. Husu, J. Laukkanen, B. Bai, M. Kuittinen, J. Turunen, and M. Kauranen, “Local field asymmetry drives second-harmonic generation in noncentrosymmetric nanodimers,” Nano Lett. **7**, 1251–1255 (2007).
- ⁸⁰R. Czaplicki, J. Mäkitalo, R. Siikanen, H. Husu, J. Lehtolahti, M. Kuittinen, and M. Kauranen, “Second-harmonic generation from metal nanoparticles: Resonance enhancement versus particle geometry,” Nano Lett. **15**, 530–534 (2015).
- ⁸¹S. Kujala, B. K. Canfield, M. Kauranen, Y. Svirko, and J. Turunen, “Multipole interference in the second-harmonic optical radiation from gold nanoparticles,” Phys. Rev. Lett. **98**, 167403 (2007).
- ⁸²X. Wu, B. Liu, T. Frauenheim, S. Tretiak, C. Yam, and Y. Zhang, “Investigation of plasmon relaxation mechanisms using nonadiabatic molecular dynamics,” J. Chem. Phys. **157**, 214201 (2022).
- ⁸³X. Wu, T. van der Heide, S. Wen, T. Frauenheim, S. Tretiak, C. Yam, and Y. Zhang, “Molecular dynamics study of plasmon-mediated chemical transformations,” Chem. Sci. **14**, 4714–4723 (2023).
- ⁸⁴S. Link and M. A. El-Sayed, “Shape and size dependence of radiative, non-radiative and photothermal properties of gold nanocrystals,” International Reviews in Physical Chemistry **19**, 409–453 (2000).
- ⁸⁵C. J. Murphy, T. K. Sau, A. M. Gole, C. J. Orendorff, J. Gao, L. Gou, S. E. Hunyadi, and T. Li, “Anisotropic metal nanoparticles: Synthesis, assembly, and optical applications,” J. Phys. Chem. B **109**, 13857–13870 (2005).
- ⁸⁶K. D. Osberg, N. Harris, T. Ozel, J. C. Ku, G. C. Schatz, and C. A. Mirkin, “Systematic study of antibonding modes in gold nanorod dimers and trimers,” Nano Lett. **14**, 6949–6954 (2014).
- ⁸⁷L. Luo, Z. Liu, J. Kong, C. G. Gianopoulos, I. Coburn, K. Kirschbaum, M. Zhou, and R. Jin, “Three-atom-wide gold quantum rods with periodic elongation and strongly polarized excitons,” Proc. Natl. Acad. Sci. (U. S. A.) **121**, e2318537121 (2024).
- ⁸⁸S. Link, M. B. Mohamed, and M. A. El-Sayed, “Simulation of the optical absorption spectra of gold nanorods as a function of their aspect ratio and the effect of the medium dielectric constant,” J. Phys. Chem. B **103**, 3073–3077 (1999).
- ⁸⁹X. López-Lozano, H. Barron, C. Mottet, and H.-C. Weissker, “Aspect-ratio- and size-dependent emergence of the surface-plasmon resonance in gold nanorods – an ab initio tddft study,” Phys. Chem. Chem. Phys. **16**, 1820–1823 (2014).
- ⁹⁰W. Wei, S. Li, J. E. Millstone, M. J. Banholzer, X. Chen, X. Xu, G. C. Schatz, and C. A. Mirkin, “Surprisingly long-range surface-enhanced raman scattering (sers) on au–ni multi-segmented nanowires,” Angewandte Chemie International Edition **48**, 4210–4212 (2009).
- ⁹¹J. Kumar, X. Wei, S. Barrow, A. M. Funston, K. G. Thomas, and P. Mulvaney, “Surface plasmon coupling in end-to-end linked gold nanorod dimers and trimers,” Phys. Chem. Chem. Phys. **15**, 4258–4264 (2013).
- ⁹²W. An, T. Zhu, and Q. Zhu, “Numerical investigation of radiative properties and surface plasmon resonance of silver nanorod dimers on a substrate,” Journal of Quantitative Spectroscopy and Radiative Transfer **132**, 28–35 (2014).
- ⁹³M. Alsawafta, “Effect of non-alignment on nearfield coupling, charge density and sensitivity to the host medium of a gold nanorod homodimer,” J. Mater. Sci. **57**, 14324–14338 (2022).
- ⁹⁴A. Slablab, L. L. Xuan, M. Zielinski, Y. de Wilde, V. Jacques, D. Chauvat, and J.-F. Roch, “Second-harmonic generation from coupled plasmon modes in a single dimer of gold nanospheres,” Opt. Express **20**, 220–227 (2012).
- ⁹⁵M. Danckwerts and L. Novotny, “Optical frequency mixing at coupled gold nanoparticles,” Phys. Rev. Lett. **98**, 026104 (2007).
- ⁹⁶S. Kovalev, R. M. A. Dantas, S. Germanskiy, J.-C. Deinert, B. Green, I. Ilyakov, N. Awari, M. Chen, M. Bawatna, J. Ling, F. Xiu, P. H. M. van Loosdrecht, P. Surówka, T. Oka, and Z. Wang, “Non-perturbative terahertz high-harmonic generation in the three-dimensional dirac semimetal cd3as2,” Nat. Commun. **11** (2020), 10.1038/s41467-020-16133-8.
- ⁹⁷G. Zograf, K. Koshelev, A. Zalogina, V. Korolev, R. Hollinger, D.-Y. Choi, M. Zuerch, C. Spielmann, B. Luther-Davies, D. Kartashov, S. V. Makarov, S. S. Kruk, and Y. Kivshar, “High-harmonic generation from resonant dielectric metasurfaces empowered by bound states in the continuum,” ACS Photonics **9**, 567–574 (2022).
- ⁹⁸D. Hähnel, C. Golla, M. Albert, T. Zentgraf, V. Myroshnychenko, J. Förstner, and C. Meier, “High-harmonic generation from resonant dielectric metasurfaces empowered by bound states in the continuum,” Light: Science & Applications **12**, 97 (2023).
- ⁹⁹M. S. Verma, M. Kumar, and M. Chandra, “Controlling second harmonic generation of gold nanorods: Surface area matters more than aspect ratio,” Chem. Phys. Lett. **741**, 137112 (2020).
- ¹⁰⁰H. M. Ngo, P. P. Nguyen, and I. Ledoux-Rak, “Optimization of second harmonic generation of gold nanospheres and nanorods in aqueous solution: the dominant role of surface area,” Phys. Chem. Chem. Phys. **18**, 3352–3356 (2016).
- ¹⁰¹C. Hubert, L. Billot, P.-M. Adam, R. Bachelot, P. Royer, J. Grand, D. Gindre, K. D. Dorkenoo, and A. Fort, “Role of surface plasmon in second harmonic generation from gold nanorods,” Appl. Phys. Lett. **90**, 181105 (2007).
- ¹⁰²J. Krauth, H. Giessen, and M. Hentschel, “Wavelength-dependent third-harmonic generation in plasmonic gold nanoantennas: Quantitative determination of the d-band influence,” ACS Photonics **5**, 1863–1870 (2018).
- ¹⁰³H. Maekawa, E. Drobnih, C. A. Lancaster, N. Large, G. C. Schatz, J. S. Shumaker-Parry, M. Sukharev, and N.-H. Ge, “Wavelength and polarization dependence of second-harmonic responses from gold nanocrescent arrays,” J. Phys. Chem. C **124**, 20424–20435 (2020).
- ¹⁰⁴C. Li, X. Lu, A. Srivastava, S. D. Storm, R. Gelfand, M. Pelton, M. Sukharev, and H. Harutyunyan, “Second harmonic generation from a single plasmonic nanorod strongly coupled to a wse2 monolayer,” Nano Lett. **21**, 1599–1605 (2021).
- ¹⁰⁵O. A. Douglas-Gallardo, M. Berdakin, T. Frauenheim, and C. G. Sánchez, “Plasmon-induced hot-carrier generation differences in gold and silver nanoclusters,” Nanoscale **11**, 8604–8615 (2019).
- ¹⁰⁶Z. Pei, Y. Mao, Y. Shao, and W. Liang, “Analytic high-order energy derivatives for metal nanoparticle-mediated infrared and Raman scattering spectra within the framework of quantum mechanics/molecular mechanics model with induced charges and dipoles,” J. Chem. Phys. **157**, 164110 (2022).
- ¹⁰⁷T. S. Julian Obermeier and M. Lippitz, “Nonlinear spectroscopy of plasmonic nanoparticles,” Adv. Phys.: X **3**, 1454341 (2018).
- ¹⁰⁸R. R. Tykwinski, U. Gubler, R. E. Martin, F. Diederich, C. Bosshard, and P. Günter, “Structure-property relationships in third-order nonlinear optical chromophores,” J. Phys. Chem. B **102**, 4451–4465 (1998).

Supporting Information:
Laser Pulse Induced Second- and Third-Harmonic Generation of Gold Nanorods with Real-Time Time-Dependent Density Functional Tight Binding (RT-TDDFTB) Method

Sajal Kumar Giri and George C. Schatz

Department of Chemistry, Northwestern University, 2145 Sheridan Road, Evanston, Illinois 60208, United States

Contents

1	Supplementary Note	S2
2	Plasmon Excited States	S2
3	Harmonic Generation	S3
4	(Hyper-)Polarizability Results	S3

arXiv:2405.00913v1 [physics.optics] 1 May 2024

1 Supplementary Note

The frequency domain polarizability is computed as

$$\alpha_{ab}(\omega) = \sum_{n>0} \left[\frac{\langle 0|\hat{\mu}_a|n\rangle\langle n|\hat{\mu}_b|0\rangle}{\omega_{n0} - \omega - i\gamma/2} + \frac{\langle 0|\hat{\mu}_b|n\rangle\langle n|\hat{\mu}_a|0\rangle}{\omega_{n0} + \omega + i\gamma/2} \right] \quad (\text{S1})$$

where $\hat{\mu}_a$ denotes the dipole moment operator along the axis a and $\omega_{n0} = \omega_n - \omega_0$ with n -th excited and ground state energies ω_n and ω_0 , respectively.

2 Plasmon Excited States

Table S1: Transition weights for Au nanorod systems from the LR-TDDFTB calculation.

Au ₇₃		Au ₉₇		Au ₁₂₁		Au ₁₄₅	
Transition	Weight	Transition	Weight	Transition	Weight	Transition	Weight
357 → 407	0.52171593	495 → 540	0.77338086	671 → 735	0.93300703	751 → 807	0.80383184
356 → 408	0.52168928	485 → 537	0.43099867	674 → 734	0.18809485	795 → 806	0.24277941
364 → 406	0.27510656	486 → 538	0.43044661	675 → 733	0.18809157	794 → 805	0.24277937
367 → 408	0.25351965	488 → 541	0.07859804	674 → 733	0.11307996	733 → 798	0.23335383
368 → 407	0.25351783	487 → 542	0.07859706	675 → 734	0.11307854	734 → 799	0.23332356
337 → 407	0.21354481	496 → 542	0.05124066	730 → 742	0.07269473	791 → 801	0.18285123
336 → 408	0.21354415	497 → 541	0.05123796	676 → 734	0.05674202	795 → 827	0.17141208
365 → 409	0.17558812	533 → 540	0.04502403	677 → 733	0.05674043	794 → 826	0.17141123
366 → 410	0.17558719	530 → 542	0.03693731	652 → 733	0.05334382	791 → 800	0.08687989
402 → 411	0.14479841	529 → 541	0.03693730	651 → 734	0.05334353	794 → 827	0.04755123
398 → 408	0.11277838	533 → 545	0.03278970	725 → 734	0.04892660	795 → 826	0.04755066
399 → 407	0.11277830	524 → 549	0.02942699	724 → 733	0.04892655	791 → 807	0.04648656
393 → 412	0.09786357	523 → 550	0.02942675	730 → 747	0.03923366	718 → 805	0.04461401
402 → 415	0.08808187	522 → 546	0.02786449	648 → 733	0.03009979	717 → 806	0.04461378
399 → 408	0.07030838	480 → 541	0.02398210	647 → 734	0.03009936	794 → 806	0.03881947
398 → 407	0.07030837	479 → 542	0.02398182	676 → 733	0.02211684	795 → 805	0.03881942

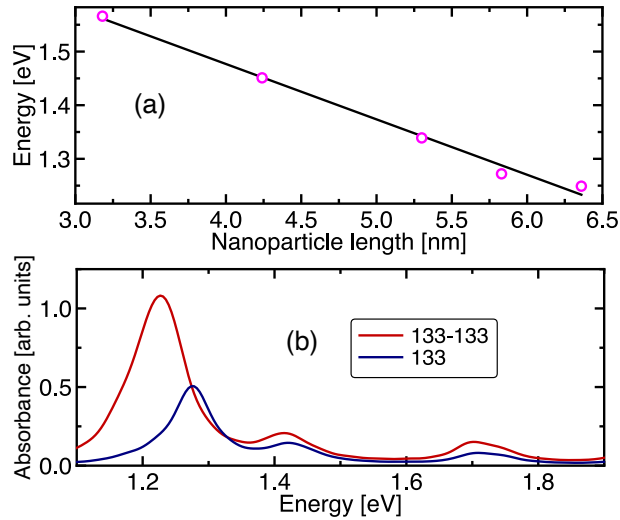


Figure S1: (a) Plasmon energy (longitudinal mode) as a function of nanoparticle length (single particle). (b) Absorption spectra for Au₁₃₃ and Au₁₃₃-Au₁₃₃ systems. Here, $h = 6\text{\AA}$ for the dimer system.

3 Harmonic Generation

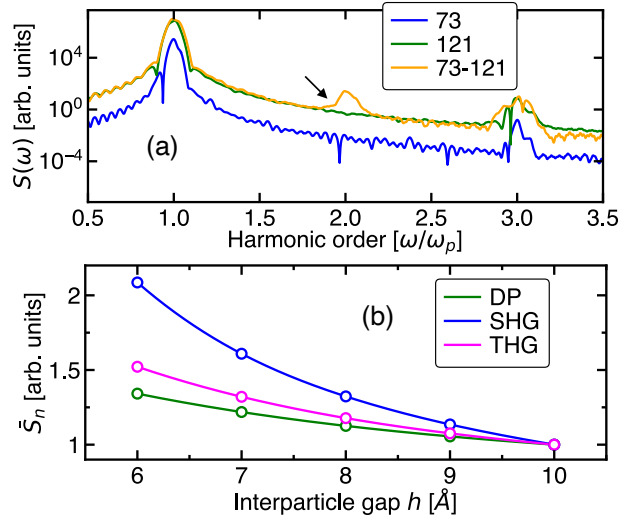


Figure S2: (a) Harmonic signals for Au₇₃, Au₁₂₁, and Au₇₃-Au₁₂₁ systems. Here, $I_p = 2.5 \times 10^8$ W/cm² and $h = 6$ Å for the dimer structure. (b) Dipole and harmonic signals as a function of inter-particle spacing. For comparison, all signals are normalized to 1 for the largest separation considered here, 10 Å. Here, $I_p = 2.5 \times 10^8$ W/cm².

4 (Hyper-)Polarizability Results

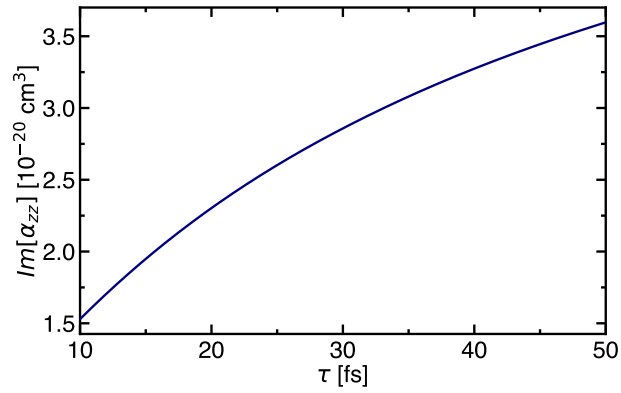


Figure S3: The ZZ polarizability component at the plasmon energy (longitudinal mode) with the decay time τ for the Au₇₃-Au₉₇ system.

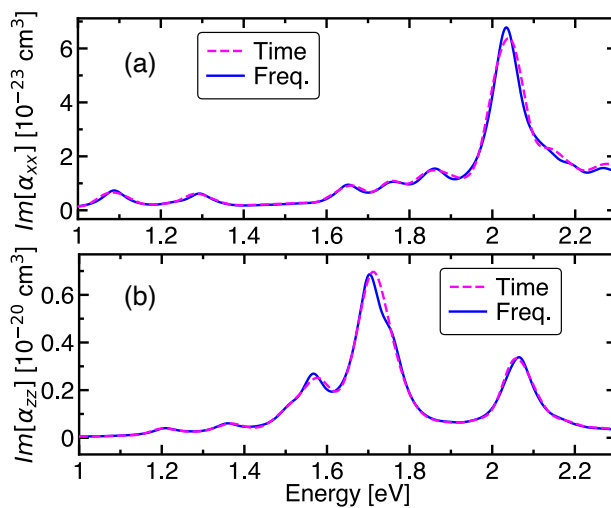


Figure S4: Comparison between time and frequency domain representations for (a) XX and (b) ZZ polarizability components for the Au_{73} system. The frequency domain polarizabilities are computed through Eq.S1 with $\gamma = 0.07$ eV.

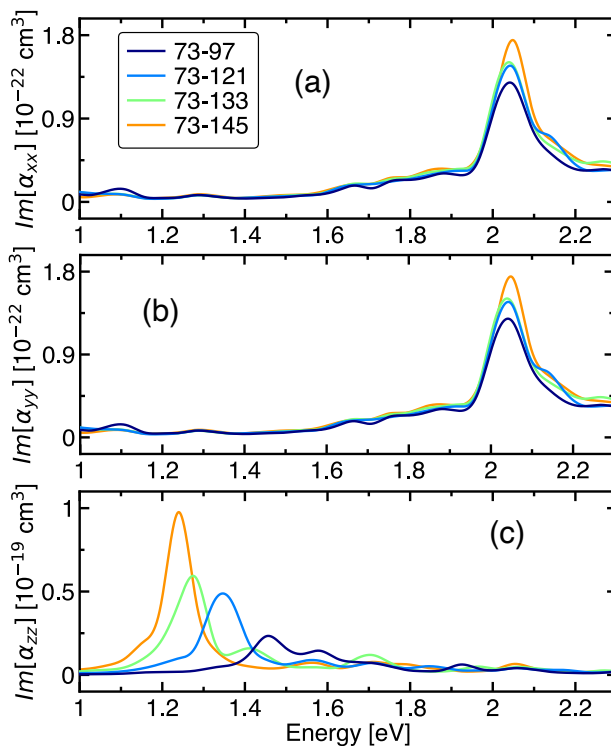


Figure S5: (a) XX , (b) YY , and (c) ZZ polarizability components for dimer systems with $h = 6 \text{ \AA}$.

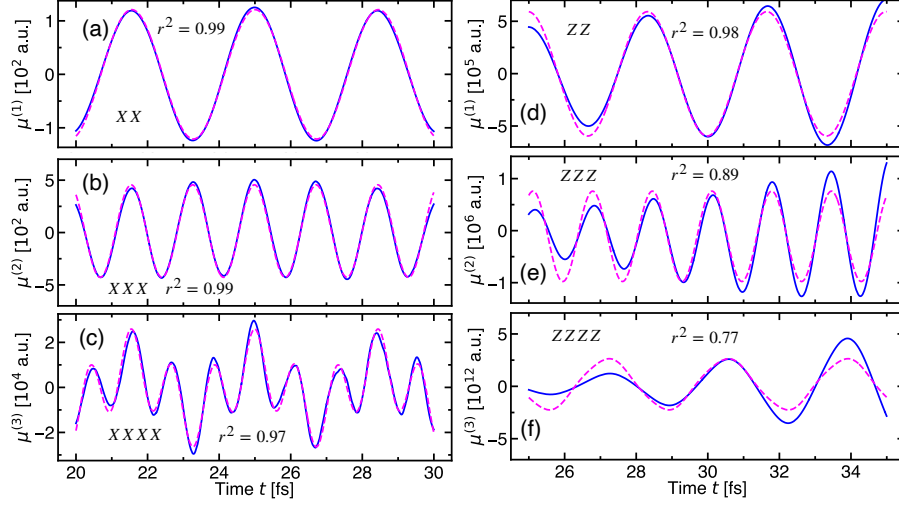


Figure S6: Fitting performed for the dipole components (a, d) $\mu^{(1)}(t)$, (b, e) $\mu^{(2)}(t)$, and (c, f) $\mu^{(3)}(t)$. The left column corresponds to the para-nitroaniline molecule (the same molecules as studied by Li and co-workers [68]), while the right column represents the Au73-Au145 system. The magenta dashed lines represent the fitting, while the blue lines denote the reference dipole components. r^2 values for the fitting are given in each subplot. We used a base intensity of 1.3×10^{11} W/cm² for the molecule, while for nanoparticles, we used 3×10^7 W/cm² for the computation of dipole components.

Table S2: (Hyper-)Polarizabilities of the para-nitroaniline molecule at $\omega = 1.2$ eV computed using RT-TDDFTB. Here, $\alpha(-\omega; \omega)$ is polarizability, $\beta(0; \omega, -\omega)$ is optical refraction, $\beta(-2\omega; \omega, \omega)$ is first hyper-polarizability, $\bar{\gamma}(-\omega; \omega, \omega, -\omega)$ indicates degenerate four-wave mixing, and $\gamma(-3\omega; \omega, \omega, \omega)$ is second hyper-polarizability. The values in the last column are taken from [68], calculated at $\omega = 1.16$ eV using the TD-DFT/6-31G(d) level of theory. Here, all results are provided in atomic units (a.u.).

$\alpha(-\omega; \omega)$	α_{xx}	121	143.82
	α_{yy}	82	90.58
	α_{zz}	0.2	29.54
$\beta(0; \omega, -\omega)$	β_{xxx}	1237	1755.39
	β_{yyy}	-110	-136.40
	β_{zzz}	-0.4	-3.66
	β_{zxx}	16	47.18
	β_{zzz}	0.02	0.95
$\beta(-2\omega; \omega, \omega)$	β_{xxx}	1766	2602.56
	β_{yyy}	175	189.24
	β_{zzz}	-0.1	-5.96
	β_{zxx}	22	58.19
	β_{zzz}	0.02	1.04
$\bar{\gamma}(-\omega; \omega, \omega, -\omega)$	$\bar{\gamma}_{xxxx}$	85606	117000.81
	$\bar{\gamma}_{zzxx}$	1048	1047.77
	$\bar{\gamma}_{xzzz}$	-0.35	-27.80
	$\bar{\gamma}_{zzzz}$	0.03	42.71
$\gamma(-3\omega; \omega, \omega, \omega)$	γ_{xxxx}	371073	428557.48
	γ_{zzxx}	3951	4267.92
	γ_{xzzz}	-0.9	-70.85
	γ_{zzzz}	0.03	47.17